Ab initio simulations of MgO under extreme conditions

Daniel Cebulla and Ronald Redmer
Institute of Physics, University of Rostock, 18051 Rostock, Germany
(Received 10 January 2014; revised manuscript received 6 March 2014; published 24 April 2014)

We determined the phase diagram of magnesium oxide with finite-temperature density functional theory molecular dynamics simulations up to temperatures and pressures as relevant for the deep interior of super-Earths and in rocky cores of giant planets such as Jupiter. The equation of state data, the Hugoniot, and a ramp compression curve are computed and compared to earlier results from diamond anvil cell and (decaying) shock wave experiments. In addition, the dynamical electrical conductivity and the reflectivity along the experimental Hugoniot curve are calculated in order to characterize electronic structure changes under compression. The structural properties of MgO are identified using pair correlation functions and self-diffusion coefficients. The solid-solid coexistence line is calculated by comparing the free enthalpies of the B1 and the B2 phase. The free energy of the solid phases is determined via thermodynamic relations using the *ab initio* simulation results and phonon calculations in the harmonic approximation. Our results indicate that the solid B2 phase of MgO does not occur in the interior of the Earth but may play an important role in super-Earths and in rocky planetary cores.

DOI: 10.1103/PhysRevB.89.134107 PACS number(s): 64.10.+h, 62.50.−p, 64.70.K−, 63.20.dk

I. INTRODUCTION

Magnesium oxide is a widely abundant mineral in the Earth's mantle. It is also expected to be a major component of super-Earths, i.e., exoplanets with up to ten Earth masses [1–3], and in rocky cores of giant planets such as Jupiter [4]. Compared to the pressure and temperature range in the Earth's mantle (the core-mantle boundary is located at about 136 GPa and 4000 K based on the preliminary reference Earth model [5,6]), values up to 20 000 K and 10 TPa are expected in super-Earths and rocky planetary cores [7,8]. These extreme conditions are, up to now, not fully accessible with experiments and, thus, theoretical calculations are needed to give predictions for the behavior of MgO at such high pressures.

Due to its simple crystal structures (NaCl for the B1 phase and CsCl for the B2 phase), MgO is a prototypical material to study solid structures and solid-solid transitions. Various *ab initio* calculations for MgO have been performed so far. Especially the determination of the B1-B2 transition [9–13] has attracted a lot of attention since these results might have a significant impact on the physical properties and the composition of planetary mantles.

In the Earth's interior, only the solid B1 phase of MgO is expected to occur. This phase is extremely stable so that it is used as pressure medium and to calibrate pressure measurements in diamond anvil cells (DACs) [12]. At room temperature the stability of this phase has been measured up to 227 GPa [14] in DACs and the melting curve between the solid B1 structure and its molten salt was observed for up to 52 GPa using heated DACs [15,16]. In addition the transition to the B2 phase was predicted by various theoretical calculations. For $T = 0$ K, values between 483 and 508 GPa were derived [12,17]. The first experimental observation of the B2 phase has been reported only recently via decaying shock compression by McWilliams *et al.* [18]. Their solid-solid transition curve is located slightly above the theoretical predictions [9,12]. Furthermore, the transition from the solid B2 structure to liquid MgO is accompanied by a nonmetal-to-metal transition indicated by a rise of the reflectivity [18]. At $T = 0$ K the metallization of the solid B2 phase is expected to occur at 20.7 TPa [12]. Most recently the B2 phase was identified in another experiment by Coppari *et al.* [19] using x-ray scattering in combination with ramp compression. They also derived a significantly higher transition pressure than predicted theoretically.

However, substantial differences between these experimental results and two-phase simulations performed by Alfè [17] and Boates and Bonev [10], and other theoretical calculations, e.g., those of Strachan *et al.* [13], Drummond *et al.* [11] or Belonoshko *et al.* [9] and de Koker and Stixrude [20] still exist which have to be resolved. A precise knowledge of the phase diagram is also necessary to determine other important properties, such as the thermal conductivity and the viscosity at pressures and temperatures exceeding the values at the Earth's core-mantle boundary [21,22] and with respect to different solid structures [3].

The goal of the present work is to give improved results for the B1-B2 transition curve based on *ab initio* simulations in combination with phonon calculations in the harmonic approximation. In doing so, we consider anharmonic contributions to the free energy and compare with the recent experiments [18,19]. The equation of state data are compared with Hugoniot results and are tabulated for a large density-temperature region (see Appendix) as relevant for the interior of the Earth and of super-Earths. In order to identify the experimentally observed nonmetal-to-metal transition, the reflectivity and the electrical conductivity of MgO are calculated for several points along the Hugoniot curve adapted from McWilliams *et al.* [18] and compared to the results of their decaying shock experiment.

II. COMPUTATIONAL METHODOLOGY

In this section, we outline the details of the *ab initio* simulations and of the other computational methods that are used to calculate the equation of state (EOS) data, the phase diagram, and the optical properties of MgO.

A. *Ab initio* simulations

We used the plane-wave code VASP (Vienna *ab initio* simulation package VASP 5.2.8) [23–25] for the finite-temperature density functional theory molecular dynamics (FT-DFT-MD) simulations to obtain thermodynamic data. Here, FT-DFT calculations [26–28] for the electronic structure are combined with classical MD simulations for the ions in the system within the Born-Oppenheimer approximation [29]. The ion temperature was controlled by a Nosé thermostat [30], and the temperature of the electrons was fixed by Fermi weighting the occupation of bands using Mermin's extension of standard DFT [28]. For the exchange-correlation contribution, the functional of Armiento and Mattsson in the generalized gradient approximation (AM05-GGA) is used, which yields improved bulk properties for solids [31,32]. In addition the AM05 functional reproduces the density of the unit cells for given experimental lattice constants best compared with other functionals such as LDA [33], PBE [34], and PBEsol [35]. To reduce the numerical efforts, projected augmented wave (PAW) pseudopotentials [36] with eight electrons for Mg ($2p^6 3s^2$) and six electrons for O ($2s^2 2p^4$) were used. As a result a qualitative estimation of the optical properties is possible and simultaneously the numerical effort is minimized.

The simulations were performed using the NVT ensemble. For given volume V and temperature T, the internal energy U and the pressure P are calculated. A plane-wave cutoff energy of 1000 eV for a supercell containing 64 ions in the B1 phase and 128 ions in the B2 phase was chosen. These calculations were performed using the Baldereschi mean value point [37] as the sampling point in the Brillouin zone. The convergence with respect to **k**-point sampling and cutoff energy was checked using up to $3 \times 3 \times 3$ Monkhorst-Pack grids [38] and 2000 eV cutoff energies on snapshots to ensure the required accuracy.

The calculations started in the low temperature regime where up to 15 000 simulation steps with 2.5–0.7 fs duration were used. The length of the time step was chosen to resolve the highest phonon frequencies in the system well. Thermodynamic equilibrium for each simulation point was ensured, e.g., at least the first 1000 time steps (few picoseconds) of the simulation runs were disregarded to guarantee equilibrated ensembles. Such converged simulation runs were also used for the initial configuration of simulations at higher temperatures. At sufficiently high temperatures, the solid structure melts and the regime of a molten salt is reached. Using this technique, the phase diagram and the EOS data presented in this work were determined.

B. Determination of the solid-solid phase transition

Since different numbers of atoms are treated in the respective supercells, a transformation from one structure to another is not possible, which prevents a direct determination of solid-solid transitions within this simulation technique. Therefore the solid-solid B1-B2 phase transition is calculated applying thermodynamic relations [39,40]. The location of the phase transition in P-T space derives from the equality of the free enthalpy of both phases $G_{\mathrm{B1}} = G_{\mathrm{B2}}$, where G is defined as

$$\begin{aligned} G_\alpha(T,P) &= U_\alpha(T,P) - TS_\alpha(T,P) + PV_\alpha(T,P) \\ &= F_\alpha(T,P) + PV_\alpha(T,P). \end{aligned} \tag{1}$$

Here, S_α is the entropy and F_α the free energy with $\alpha =$ B1, B2. The variables of the free enthalpy G_α are temperature T and pressure P so that we switched from the NVT ensemble used in the FT-DFT-MD simulations to a NPT representation by interpolating the volume V, the internal energy U and the entropy S on a fine P-T grid. The free enthalpy is determined on each grid point for both solid structures. By calculating the change of the free enthalpy ΔG the corresponding transition pressure P_{tr} follows from the condition that ΔG is zero for a given temperature:

$$\begin{aligned} \Delta G &= G_{\mathrm{B1}} - G_{\mathrm{B2}} \\ &= (F_{\mathrm{B1}} - F_{\mathrm{B2}}) + P_{\mathrm{tr}}(V_{\mathrm{B1}} - V_{\mathrm{B2}}) = 0. \end{aligned} \tag{2}$$

Here, we start from the basic assumption that the free energy F_α, the internal energy U_α as well as the entropy S_α consist of ionic, electronic, and electron-phonon contributions [39]. In this work we take into account the dominating contributions of the ion lattice vibrations and the electronic fraction (el) [39]. The influence of electron-phonon contributions on the entropy and the internal energy is neglected. The phonon contribution can be decomposed into harmonic ion motions (ph) and an anharmonic motion part (anh), which becomes important for higher temperatures up to the region where melting occurs:

$$F(T,V) = \Phi_0(V) + F_{\mathrm{ph}}(T,V) + F_{\mathrm{anh}}(T,V) + F_{\mathrm{el}}(T,V). \tag{3}$$

$\Phi_0(V)$ represents the electronic ground-state energy. All three contributions to the internal energy U are calculated *ab initio* within the FT-DFT-MD simulations: the electronic contribution follows from the DFT calculations, while the ion motion is described by Newton's equation of motion. Due to the classical treatment of the ion motion at low temperatures, quantum effects like the zero-point vibrational energy are not taken into account. Furthermore, the entropy has to be calculated separately.

C. Phonons and harmonic approximation

In simplest approximation, we only consider the electronic ground-state energy and the harmonic motion of the ions (phonons). The additional electronic energy due to excitations is two orders of magnitude smaller than the contribution of the ion motion, and the neglect of the anharmonicities is valid for temperatures far below melting where only small displacements of the atoms from their equilibrium lattice positions can be assumed [39]. This leads to the *quasiharmonic approximation* for which analytical results for the internal energy U_{ph} and the entropy S_{ph} are known. In this case it is only necessary to calculate the phonon frequencies $\omega_r(\mathbf{k})$ in dependence of the band number r ($r = 1, \ldots, 3N$) and **k** vector of the N ions in the respective unit cell ($N = 2$ for both

solid phases of MgO),

$$F_{\rm ph}(T,V) = \sum_{\mathbf{k},r} \frac{1}{2}\hbar\omega_r(\mathbf{k},V) - \frac{1}{\beta}\sum_{\mathbf{k},r} \ln\{1-\exp[-\beta\hbar\omega_r(\mathbf{k},V)]\}, \quad (4)$$

$$S_{\rm ph}(T,V) = -\left.\frac{\partial F_{\rm ph}(T,V)}{\partial T}\right|_V, \quad (5)$$

$$U_{\rm ph}(T,V) = F_{\rm ph}(T,V) + T S_{\rm ph}(T,V), \quad (6)$$

$$P_{\rm ph}(T,V) = -\left.\frac{\partial F_{\rm ph}(T,V)}{\partial V}\right|_T. \quad (7)$$

Here, $\beta = 1/k_B T$ represents the inverse temperature. The calculation of the phonon frequencies $\omega_r(\mathbf{k},V)$ in the quasiharmonic approximation is performed using the PHONOPY code [41]. The forces are derived within the finite displacement method [42,43]. PHONOPY uses VASP to calculate the forces. Therefore a static DFT calculation at 0 K is necessary to determine the dynamic matrix (the matrix of the second derivatives of the interatomic potential in the harmonic approximation). The ground-state energy $\Phi_0(V)$ is taken from the static DFT calculations as well. In a second step, the phonon frequencies are calculated by solving the second order differential equation of the harmonic oscillator model [39,41]. The volume dependence in Eqs. (3)–(6) is introduced by calculating up to 20 different isochors for both solid phases.

Similar to the above mentioned procedure the convergence was also checked for the DFT and phonon calculations at $T = 0$ K with respect to **k**-point sampling and the cutoff energy. A cutoff energy of 1000 eV and a $2\times2\times2$ **k**-point grid were used for the VASP calculations (checked against 2000 eV and a $5\times5\times5$ Monkhorst-Pack grid). The thermodynamic data of the phonon calculations were also derived using a Monkhorst-Pack **k**-point grid [38], in fact, a much denser grid of $51\times51\times51$ (checked against a $100\times100\times100$ **k**-point grid). In this way, the accuracy of the numerical results is guaranteed to be better than 0.1%. Within these approximations, the B1-B2 transition curve of MgO can be calculated using the thermodynamic values determined by PHONOPY based on Eqs. (5) and (6) and the DFT calculations for $T = 0$ K. By interpolating the free enthalpy G the B1-B2 transition pressure is determined for given temperatures. In this case, the change of the free enthalpy contains no anharmonic contributions.

Due to the use of the quasiharmonic approximation, the quantum zero-point vibrational energy is included, while anharmonicities are still neglected. The treatment of the latter contributions is described in Sec. II D.

D. Calculation of the anharmonic free energy

With the FT-DFT-MD data the calculation of the free energy F can be performed. Compared to the free energy within the quasiharmonic approximation the *ab initio* simulations include anharmonicities in a genuine way. Inserting

$$\left.\frac{\partial F}{\partial T}\right|_V = \frac{F}{T} + T\left.\frac{\partial(F/T)}{\partial T}\right|_V \quad (8)$$

into the definition of the free energy $F = U + T\frac{\partial F}{\partial T}|_V$, an equation, which can be evaluated numerically to derive the free energy at a given temperature along isochores:

$$U = -T^2\left.\frac{\partial(F/T)}{\partial T}\right|_V, \quad (9)$$

is found. The anharmonic contributions can be separated via

$$U_{\rm anh} = U_{\text{FT-DFT-MD}} - U_{\rm ph} - \Phi_0, \quad (10)$$

and the anharmonic free energy at a temperature T_f is then given by the following expression:

$$F_{\rm anh}(T_f)|_V = F_{\rm anh}(T_i)|_V \frac{T_f}{T_i} - T_f\int_{T_i}^{T_f}\left.\frac{U_{\rm anh}(T)}{T^2}\right|_V dT. \quad (11)$$

The free energy at a final temperature $F_{\rm anh}(T_f)|_V$ for a constant volume V is calculated relative to the free energy at an initial temperature $F_{\rm anh}(T_i)$. For low enough T_i, anharmonicities can be neglected and the free energy $F_{\rm anh}(T_i)$ vanishes there. The resulting transition curve is connected with the coexistence curve of the harmonic approximation at T_i that is chosen high enough to include the quantum effects from the quasiharmonic approximation but also below the region where anharmonicities appear. A reasonable compromise is $T_i = 3000$ K.

E. Reflectivity and dynamical electrical conductivity

A detailed analysis of the B1-B2 and B2-liquid transitions reported by McWilliams *et al.* [18] can be performed by calculating the reflectivity for several states along the experimental Hugoniot curve. In addition, the nonmetal-to-metal transition that should occur simultaneously with the B2-liquid transition might give us new insights into the origin and the shape of planetary magnetic fields of, e.g., hot super-Earths.

Using the Kubo-Greenwood formula [44,45], the real part of the dynamic electrical conductivity $\sigma(\omega)$ can be calculated for a number of snapshots (we have chosen 20) to determine statistically averaged results [46–48]:

$$\sigma(\omega) = \left\langle \frac{2\pi e^2}{3m^2\omega\Omega}\sum_{\mathbf{k}}\sum_{i,j=1}^{N_B}\sum_{\alpha=1}^{3}[f(\epsilon_{i\mathbf{k}}) - f(\epsilon_{j\mathbf{k}})] \times |\langle\psi_{j\mathbf{k}}|\hat{\mathbf{p}}|\psi_{i\mathbf{k}}\rangle|^2\delta(\epsilon_{j\mathbf{k}} - \epsilon_{i\mathbf{k}} - \hbar\omega)\right\rangle. \quad (12)$$

Here, Ω is the volume of the supercell, $\langle\psi_{j\mathbf{k}}|\hat{\mathbf{p}}|\psi_{i\mathbf{k}}\rangle$ the transition matrix elements over all electronic bands N_B of the Kohn-Sham orbitals multiplied by a broadening function and the respective thermal occupation numbers $f(\epsilon_{i\mathbf{k}})$ (Fermi weighting).

With the Kramers-Kronig relation the imaginary part of the dynamic electrical conductivity is determined. The dielectric function is derived and the index of refraction $n(\omega) + ik(\omega)$ is evaluated. Finally the reflectivity $R(\omega)$ is calculated using

the Fresnel formula [49]:

$$R(\omega) = \frac{[n_0 - n(\omega)]^2 + [k_0 - k(\omega)]^2}{[n_0 + n(\omega)]^2 + [k_0 + k(\omega)]^2}. \quad (13)$$

Equation (12) was evaluated considering 2000 electronic bands, a 1000 eV cutoff energy, and a $3 \times 3 \times 3$ Monkhorst-Pack **k**-point grid [38]. The accuracy of the results was checked against cutoff energies up to 2000 eV and a $5 \times 5 \times 5$ **k**-point grid. We switched to PAW-GW pseudopotentials due to the fact that the projectors, which play a major role in the calculation of the optical properties, were optimized for these pseudopotentials. To ensure a sufficiently large number of bands the number of atoms in the B2 phase was reduced to 54 atoms.

Compared to the experimental data of the decaying shock experiment of McWilliams *et al.* [18] one has to keep in mind that $n_0 = 1.743$ ($k_0 = 0$) represents the index of refraction of MgO [50] at normal conditions. Additional reflections at the MgO-vacuum boundary can be neglected due to the use of an antireflecting coating at this surface in the experimental setup [18].

III. RESULTS

The FT-DFT-MD simulation described in the previous section were used to calculate accurate EOS data in the region from 500 to 20 000 K and pressures up to 1.5 TPa, which are relevant for the interior of the Earth and of super-Earths. The corresponding data for the pressure and the internal energy are given in Appendix and may be used for constructing improved interior models for planets [3,7]. An overall survey of these results is given in the pressure-temperature diagram, Fig. 1. The black squares of the solid B1 phase are separated from the green diamonds of the B2 phase by the corresponding coexistence curve. The white area between the solid structures and the liquid phase (red circles) represents the region where the solid-liquid transition is expected. An exact determination of the solid-liquid transition curve is, contrary to that of the B1-B2 transition, not possible within our method due to the appearance of an amorphous structure in the transition region, see Sec. III A.

We identify the different phases by using the pair correlation functions (see Fig. 2), i.e., we compare the averaged pair correlation function of the different phases with the ideal crystal structures at the same density. Furthermore, a diffusion analysis is performed and the mean square displacement of the ions is determined in order to distinguish the liquid phase from the solid phases. When thermodynamic equilibrium for a solid structure is reached (i.e., the simulation is converged) the slope of the mean square displacement during the simulation is close to zero and only small vibrations of the ions around their equilibrium positions are visible. For the liquid phase, the ions can diffuse freely through the simulation box, resulting in a significant rise of the slope of the mean square displacement along the simulation time by up to nine orders of magnitude.

A. Melting and solid-liquid transition

The liquid phase is reached by melting of the solid structures. With increasing temperature the displacements

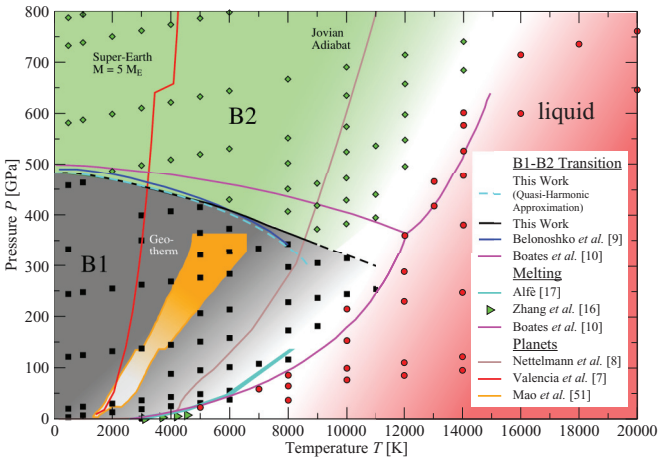

FIG. 1. (Color) Phase diagram of MgO up to a pressure of 800 GPa and a temperature of 20 000 K. The B1 phase is represented by the black squares, the B2 phase by the green diamonds, and the liquid phase by red circles. B1-B2 coexistence curves; black line-present result, blue line-Belonoshko *et al.* [9], and magenta line(s)-Boates and Bonev [10]. The solid B1-liquid transition is in good agreement with the results of Alfè [17] and with the experiments of Zhang *et al.* [16]. The geotherm [51] indicates that under Earth's interior conditions only the B1 phase is found. In a super-Earth with, e.g., 5 M_E [7] the B2 phase may exist even in the mantle (indicated by the kink in the red curve). For comparison, the Jupiter adiabat [8] is also shown.

of the ions from the ideal lattice position becomes larger and finally the ions can diffuse freely through the volume (simulation box). Between the solid and the liquid phases, the pair distribution function indicates an amorphous structure,

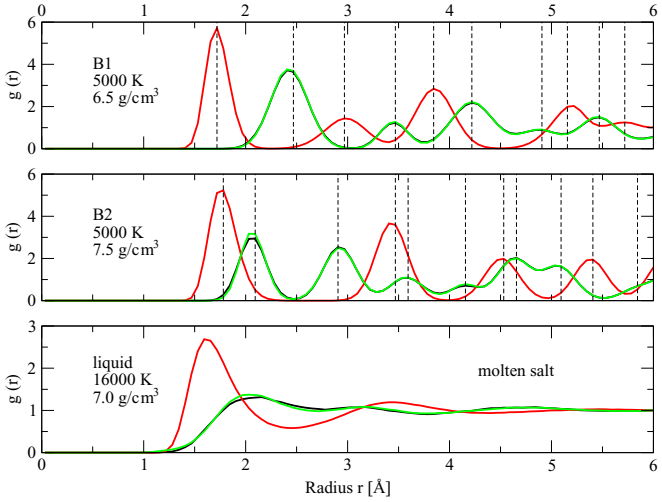

FIG. 2. (Color online) Structure identification by means of pair correlation functions: $g_{\text{Mg-O}}$ (red line), $g_{\text{Mg-Mg}}$ (green line), $g_{\text{O-O}}$ (black line). The vertical black dashed lines in the upper two panels mark the ion positions of an ideal MgO crystal in the B1 structure (top) or the B2 structure (middle). The peaks in the top (middle) diagram agree with the ion positions in an ideal B1 (B2) MgO crystal. The bottom diagram shows the behavior of a dense liquid or, as in this case, a molten salt.

which is neither solid nor liquid (represented by the white area in Fig. 1). This artificial amorphous structure results from the finite-sized supercell; the periodic boundary conditions lead to a hysteresis effect and an overheated solid is reached which instantaneously melts at temperatures above the *true* melting temperature. When refreezing the liquid phase, an undercooled liquid is reached and the melting temperature is underestimated. The latter feature was not observed in our simulations due to the fact that refreezing always leads to an amorphous solid structure and the original crystal structure was not recovered.

Experimental measurements of the solid-liquid transition curve from heated DACs [15,16] lead to results, which agree well [16] with our estimates for that region. Our predictions for the solid-liquid transition region are also in good agreement with the more adequate two-phase simulation results of Alfè [17] and those of Boates and Bonev [10]. For the melting of the B2 phase, the simulation lead at higher pressures to a region close to the results of Boates and Bonev [10]. Other suggestions for the B2-liquid transition based on estimates for the Clausius-Clapeyron slope $dP/dT = \Delta S/\Delta V$ at the triple point give a rough impression and can be found in literature [9,13] (see Fig. 1).

B. B1-B2 transition curve

In Fig. 1, the different theoretical curves for the B1-B2 transition are shown. The dashed light blue line is obtained within the quasiharmonic approximation [Eq. (2) without anharmonicities]. The black curve represents the results combining FT-DFT-MD simulations with phonon calculations as described in Sec. II D.

At $T = 0$ K, the resulting transition pressure of 483 GPa is close to other theoretical results of Belonoshko *et al.* [9], Oganov *et al.* [12], Alfè [17], and Boates and Bonev [10]. The quasiharmonic approximation leads to a good estimation for the B1-B2 transition at low temperatures and the agreement with the results of the quasiharmonic approximation of Belonoshko *et al.* [9] with the calculation of the phonon-based free energy by integrating over the phonon density of states (DOS) is obvious. With increasing temperature the anharmonic ion motion plays a more important role. It leads to higher transition pressures at higher temperatures compared with the harmonic approximation.

The calculated transition curve is in good agreement with other theoretical results, e.g., that of Belonoshko *et al.* [9] who derived the transition line, in addition to the quasiharmonic approximation mentioned above, from two-phase simulations and the Z method. Similar results were provided by Oganov *et al.* [12] who determined the transition by integrating the Clausius-Clapeyron slope with an initial value for the transition pressure for $T = 0$ K that was also calculated. The difference to the recently published two-phase simulations of Boates and Bonev [10] increases with temperature. An explanation for this disagreement might be the sampling of the Brillouin zone: they used only the Γ point which leads to slightly different P and U values as our detailed convergence checks have shown.

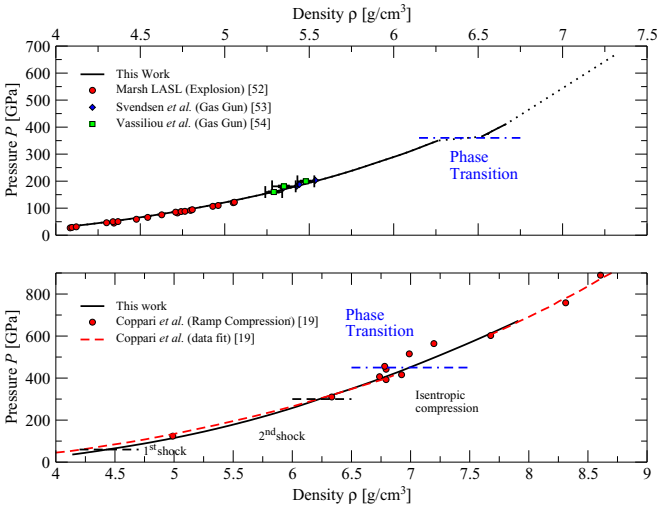

FIG. 3. (Color online) Hugoniot curve (top) and ramp compression path (bottom). Black lines represent the results of the present work. (a) Hugoniot curve (top). For densities up to 5.5 g/cm^3 very good agreement with shock wave experiments of Marsh (red circles [52]), Vassiliou *et al.* (blue diamonds [54]) and Svendsen *et al.* (green squares [53]) is obtained. The kink at 6.25 g/cm^3 is due to phase transition from B1 to B2. (b) Ramp compression experiment of Coppari *et al.* [19] (bottom). The red data points and their fit agree nicely with our theoretical predictions.

C. Hugoniot curve and ramp compression

Shock-wave experiments are used to probe extreme states of matter. The Hugoniot curve represents all thermodynamic states (U, P, ρ) that can be reached for given initial conditions of density, temperature, and pressure (U_0, P_0, ρ_0). Based on the FT-DFT-MD simulation data the Hugoniot curve can be calculated evaluating the Hugoniot equation,

$$U - U_0 = \frac{1}{2}(P + P_0)\left(\frac{1}{\rho_0} - \frac{1}{\rho}\right). \qquad (14)$$

The results shown in Figs. 3 and 4 are in very good agreement with the experiments of Marsh [52], Svendsen *et al.* [53] and Vassiliou *et al.* [54] for the B1 phase (Fig. 3 for $\rho_0 =$ 3.58 g/cm^3 and room temperature). Our data indicate a density jump from 6.25 g/cm^3 to 6.5 g/cm^3 when the B1-B2 transition is reached along the Hugoniot.

The first experimental observation of the solid B2 phase and of the B2-liquid transition in MgO was derived from decaying shock experiments [18]. Through time-resolved measurements of the emission, the velocity as well as the reflectivity of the shock front, the properties of the compressed MgO target were determined. In this way measurements up to 1.4 TPa and 50 000 K were performed, see Figs. 3 (top) and 4 up to 20 000 K and 800 GPa. Good agreement with earlier shock data for the B1 phase is visible in the lower part of the McWilliams *et al.* results but large differences between our calculated Hugoniot curve and their results for the B2 phase have to be stated. Between 11 000 and 14 000 K, the calculated Hugoniot curve runs right through the coexistence region between the solid B2 and the liquid phase and, due to the lack of data points in this region, only a rough estimate is possible. For temperatures

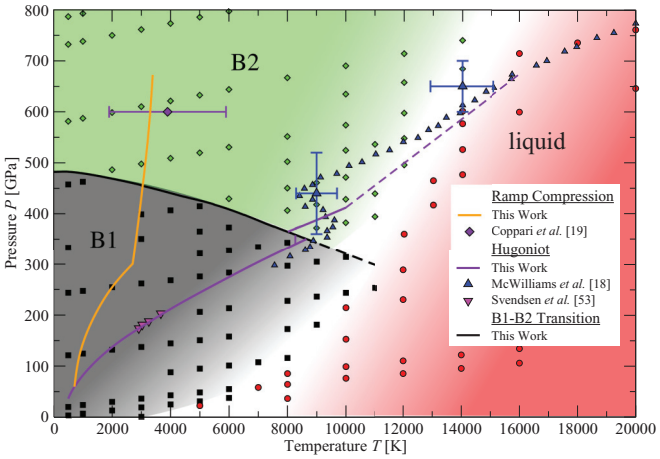

FIG. 4. (Color) Phase diagram of MgO up to a pressure of 800 GPa and a temperature of 20 000 K. The purple line is the calculated Hugoniot curve across the whole phase diagram. The extension of the Hugoniot curve (dashed purple line) runs right through the coexistence region between solid B2 phase and liquid MgO. The results of McWilliams *et al.* [18] are indicated by blue triangles. At lower temperatures, the orange curve represents our theoretical ramp compression curve calculated by two subsequent shock compressions followed by an isentrope (see the two kinks). The transition determined by Coppari *et al.* [19] is the purple diamond.

above 14 000 K, our theoretical prediction for the Hugoniot curve is again close to the measurements of the decaying shock experiments of the liquid phase. The disagreement with the experimental results in the B2 phase is still under investigation.

Based on our theoretical results, we predict that the Hugoniot follows the coexistence curve between the solid B2 and the liquid phases from about 440 to 600 GPa. For the clarification of this disagreement, further more detailed theoretical analyses and experimental data are necessary.

To investigate the transition curve at lower temperatures than the Hugoniot curve, one can use the ramp compression technique, i.e., compressing the system almost isentropically. This can be achieved by performing reverberating shock wave experiments or, in case of laser-driven compression, by pulse shaping. For instance, the experimental path can be approximated by a second shock that starts from the principal Hugoniot curve and subsequent by an isentrope, see Fig. 4. The path of the real ramp compression experiment of Coppari *et al.* [19] is presented in Figs. 3 (bottom) and 4. The ramp compression curve is constructed by combining a second shock, starting at 30 GPa and 700 K on the principle Hugoniot curve, with an isentropic compression starting at 300 GPa and 2700 K, see Ref. [19]. The structure of the B2 phase was observed using x-ray scattering. They located the B1-B2 transition at 600 GPa and 3900 K, which is significantly higher than our calculation. A possible explanation is the appearance of an amorphous structure between 420 and 600 GPa (hysteresis) that could have been observed in this experiment. Nevertheless, the calculated ramp compression curve following [19] (see Fig. 4, orange curve) is in very good agreement with the experimental point of Coppari *et al.* [19].

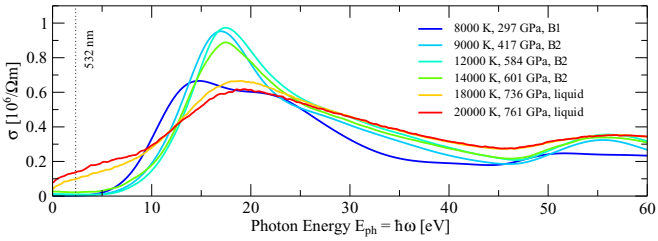

FIG. 5. (Color online) The different curves represent the electrical conductivity $\sigma(\omega)$ along the measured Hugoniot curve of McWilliams *et al.* [18]. With increasing temperature and pressure the smearing due to ionization processes increases. The plateau, which can be identified in the curves at about 55 eV, are due to the ionization of the $2p$ electrons of Mg.

D. Reflectivity and electrical conductivity

For six points along the experimental Hugoniot curve of McWilliams *et al.* [18], EOS points from our simulations were used and the real part of the dynamic electrical conductivity $\sigma(\omega)$ was calculated dependent on the photon energy, see Fig. 5. For increasing photon energy, the electrical conductivity rises due to the various inter atomic transitions and ionization processes of Mg and O. The transitions of both elements overlap, which leads to the first broad peak at about 20 eV. For higher energies, the peak decreases until at about 50 eV all electrons of the $3s$ shell of the Mg atom are ionized and the first electrons of the $2p$ shell ionize. Higher photon energies are not treated correctly in this pseudopotential formalism and are thus omitted.

Notice that our evaluation of the Kubo-Greenwood formula, Eq. (12), gives just a qualitative explanation of the behavior of the dynamic conductivity because the GGA-AM05 functional underestimates the electronic band gap and thus leads to increased values for the electrical conductivity $\sigma(\omega)$. Furthermore, a better treatment of unoccupied bands, e.g., within the GW formalism or with other exchange correlation functionals, is needed for more accurate results (see Sec. II E). However, this is beyond the scope of the current work.

The reflectivity R calculated from the electrical conductivity using Eq. (13) is slightly higher than the measured reflectivity of McWilliams *et al.* [18], see Fig. 6, which is due to the overestimated electrical conductivity.

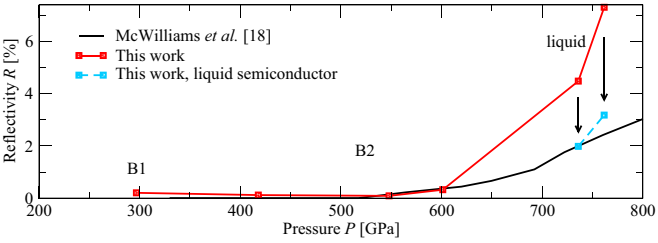

FIG. 6. (Color online) The red curve represents the calculated reflectivity R, which is compared to the Drude fit from McWilliams *et al.* [18] (black line). For the points in the liquid phase, a semiconductor model [55,56] according to Eq. (15) is applied to correct for the band-gap problem of the DFT calculations (light blue points, the resulting shift is indicated by arrows).

The wide band gap for the solid phase leads to a reflectivity close to zero. In the liquid phase, the reflectivity is higher and increases further with increasing pressure and temperature; the difference between the experimental data and the calculated values using the GGA-AM05 functional are substantial. Therefore we apply a simple liquid semiconductor model [55,56] to empirically correct the underestimated band gaps derived from DFT and to give more realistic estimates for the electrical conductivity and reflectivity in the liquid phase,

$$\sigma = \sigma_0 \exp\left[-\frac{E_g(\rho)}{2k_B T} + X\right], \tag{15}$$

with the quantity X,

$$X = -\frac{E_g^{\mathrm{exp}}(\rho_0) - E_g^{\mathrm{DFT}}(\rho_0)}{2k_B T} = \mathrm{const.} \tag{16}$$

Here, $E_g^{\mathrm{exp}}(\rho_0) = 7.83$ eV is taken from Ref. [57] and a static DFT calculation for the same density ρ_0 yields $E_g^{\mathrm{DFT}}(\rho_0) = 4.83$ eV. The corrected conductivity along the liquid branch of the Hugoniot curve results in higher reflectivities and a much better agreement with the experimental data is obtained, see Fig. 6.

A more precise analysis would require improved DFT calculations for the reflectivity using, e.g., the hybrid functional of Heyd *et al.* [58] which are much more challenging with respect to computer capacity and thus remain subject of future work; for instance, see [59].

IV. CONCLUSION

We performed extensive *ab initio* calculations for MgO using FT-DFT-MD simulations in order to derive accurate EOS data up to extreme pressures and temperatures as expected in the mantle of super-Earths and in cores of giant planets. Our data are in very good agreement with shock wave experiments (Hugoniot data and ramp compression), see Fig. 3. Furthermore, we determined the high-pressure phase diagram of MgO via basic thermodynamic relations (Gibbs free energy), by calculating the pair distribution functions and performing a diffusion analysis for the solid (B1 and B2) and liquid phases.

Compared with previous work we considered anharmonic contributions in both solid phases so that a consistent prediction for the B1-B2 transition can be given. For low temperatures, our result is in good agreement with earlier theoretical findings based on the quasiharmonic approximation [9]. For higher temperatures, the anharmonic contributions are essential, see Fig. 1. Our prediction for the B1-B2 transition line differs from that of Boates and Bonev [10]. They used the Γ point for sampling the Brillouin zone while in this work higher k-point sets were taken into account, leading to well-converged results. Furthermore, their phase diagram is based on only few points, which in fact, enables a qualitative but rough estimate for the slope for the coexistence lines.

Recent experiments reported higher pressures for the B1-B2 transition. The differences between these new experimental results and the theoretical predictions have to be clarified in future work. For instance, the experiment of Coppari *et al.* [19] might have probed an amorphous phase between 420–600 GPa. The difference to the results of McWilliams *et al.* [18] is still enigmatic but the inclusion of anharmonicities leads to a slightly better agreement with these experiments. The estimated region for melting agrees well with the different theoretical and experimental predictions but further analysis is necessary. Especially accurate Hugoniot points up to extreme pressure would be helpful, see Fig. 3.

The results for the dynamic electrical conductivity indicate that a complex ionization behavior occurs in the crystal structures and in the liquid at high pressures. More accurate results require DFT calculations using a hybrid exchange-correlation functional, e.g., that of Heyd *et al.* [58,60,61], which is computationally much more demanding and beyond the scope of the present work. Instead, we applied a simple semiconductor model [55] that corrects the DFT band gaps and leads to reasonable agreement with the reflectivities in the high-pressure liquid. The increase in the reflectivity with pressure (and temperature) indicates the occurrence of a nonmetal-to-metal transition. This effect might have an impact on the interior and the magnetic field properties of hot super-Earths.

Furthermore, the structural changes along the solid-solid transition will affect heat transport from the planetary core to the outer layers, especially due to different viscosities in these phases. This may also be important for the question whether or not plate tectonics is relevant for super-Earths [3,62]. Finally, to improve interior models for super-Earths, other compounds like SiO_2, $MgSiO_3$, FeO, and FeS have to be treated as well, and especially their mixtures [10].

ACKNOWLEDGMENTS

We thank Martin French for many helpful ideas and comments that have improved this work substantially. We also thank Manuel Schöttler, Mandy Bethkenhagen, and Andreas Becker for many lively discussions. This study was supported by the DFG within the SFB 652. The calculations were performed at the Computational Center of the University of Rostock and at the Northern German Supercomputing Alliance (HLRN).

APPENDIX: EQUATION OF STATE

The EOS data derived from the FT-DFT-MD simulations is presented in Table I. As mentioned in Sec. III the different phases were identified using averaged pair correlation function to distinguish the solid phases and the diffusion analysis to characterize the liquid phase.

TABLE I. Equation of state data for MgO up to 20 000 K and pressures up to 1.5 TPa.

ρ (g/cm^3)	T (K)	P (GPa)	u (kJ/g)	Phase
3.550	500	3.236	− 25.560	B1
3.884	500	19.951	− 25.366	B1
5.076	500	121.169	− 21.879	B1
5.983	500	243.681	− 16.751	B1
6.500	500	332.971	− 13.021	B1
7.120	500	457.495	− 7.786	B1
8.000	500	581.542	− 0.030	B2

TABLE I. *(Continued.)*

ρ (g/cm^3)	T (K)	P (GPa)	u (kJ/g)	Phase
8.600	500	732.333	5.623	B2
8.800	500	786.852	7.614	B2
3.550	1000	6.754	−24.944	B1
3.884	1000	23.880	−24.734	B1
5.076	1000	124.570	−21.247	B1
5.983	1000	247.325	−16.12	B1
7.120	1000	462.744	−7.192	B1
8.000	1000	587.263	0.587	B2
8.600	1000	738.300	6.239	B2
8.800	1000	792.939	8.238	B2
3.550	2000	12.921	−23.715	B1
3.884	2000	29.895	−23.491	B1
5.076	2000	132.005	−19.958	B1
5.983	2000	254.618	−14.801	B1
7.500	2000	486.412	−2.493	B2
8.000	2000	598.645	1.826	B2
8.600	2000	750.028	7.477	B2
8.800	2000	805.145	9.486	B2
3.000	3000	0.524	−22.057	B1
3.550	3000	19.019	−22.485	B1
3.884	3000	36.305	−22.243	B1
5.076	3000	137.475	−18.737	B1
5.983	3000	262.006	−13.630	B1
6.500	3000	350.417	−9.899	B1
6.750	3000	398.89	−7.898	B1
7.500	3000	497.834	−1.253	B2
8.000	3000	610.159	3.069	B2
8.600	3000	761.461	8.720	B2
8.800	3000	816.956	10.713	B2
3.550	4000	24.829	−21.219	B1
3.884	4000	42.790	−20.996	B1
4.511	4000	87.900	−19.658	B1
5.076	4000	144.534	−17.495	B1
5.983	4000	268.254	−12.372	B1
6.750	4000	406.857	−6.649	B1
7.500	4000	508.86	−0.014	B2
8.000	4000	621.382	4.309	B2
8.600	4000	773.395	9.965	B2
8.800	4000	828.585	11.961	B2
3.000	5000	22.432	−17.464	liquid
3.550	5000	30.956	−19.885	B1
3.884	5000	48.451	−19.731	B1
4.511	5000	95.020	−18.394	B1
5.076	5000	150.708	−16.215	B1
5.513	5000	206.228	−13.994	B1
5.983	5000	275.818	−11.099	B1
6.250	5000	321.313	−9.241	B1
6.500	5000	364.940	−7.369	B1
6.750	5000	414.744	−5.374	B1
7.500	5000	519.694	1.229	B2
8.000	5000	632.655	5.558	B2
8.600	5000	785.700	11.215	B2
8.800	5000	840.721	13.210	B2
10.000	5000	1215.624	26.184	B2
11.000	5000	1587.492	38.233	B2
3.550	6000	37.631	−18.435	B1
3.884	6000	54.911	−18.348	B1

TABLE I. *(Continued.)*

ρ (g/cm^3)	T (K)	P (GPa)	u (kJ/g)	Phase
4.511	6000	101.037	− 17.064	B1
5.076	6000	157.875	− 14.92	B1
5.513	6000	213.434	− 12.694	B1
5.983	6000	283.326	− 9.792	B1
6.250	6000	327.574	− 7.950	B1
6.500	6000	372.979	− 6.116	B1
7.000	6000	429.477	− 1.471	B2
7.500	6000	530.583	2.468	B2
8.000	6000	643.900	6.801	B2
8.600	6000	797.408	12.462	B2
8.800	6000	852.734	14.456	B2
3.550	7000	58.216	− 13.927	liquid
4.511	7000	107.552	− 15.655	B1
6.250	7000	334.236	− 6.652	B1
3.000	8000	36.511	− 12.704	liquid
3.550	8000	64.282	− 12.235	liquid
3.884	8000	85.238	− 11.734	liquid
4.511	8000	115.799	− 14.111	B1
5.076	8000	172.624	− 12.172	B1
5.513	8000	227.772	− 9.979	B1
5.983	8000	296.799	− 7.120	B1
6.250	8000	343.049	− 5.289	B1
6.762	8000	406.459	− 0.648	B2
7.000	8000	450.325	1.068	B2
7.263	8000	502.238	3.091	B2
7.500	8000	551.673	5.006	B2
8.000	8000	666.869	9.330	B2
8.600	8000	820.566	14.994	B2
8.800	8000	876.318	16.979	B2
5.076	9000	181.055	− 10.604	B1
5.513	9000	236.132	− 8.480	B1
5.983	9000	304.750	− 5.725	B1
6.499	9000	371.954	− 1.089	B2
6.762	9000	417.921	0.693	B2
7.000	9000	460.902	2.387	B2
3.550	10 000	76.097	− 8.875	liquid
3.884	10 000	98.860	− 8.213	liquid
4.511	10 000	152.712	− 6.298	liquid
5.076	10 000	214.429	− 3.875	liquid
5.513	10 000	243.645	− 6.884	B1
5.983	10 000	314.087	− 4.201	B1
6.499	10 000	382.385	0.33	B2
6.762	10 000	428.500	2.095	B2
7.000	10 000	471.407	3.747	B2
7.263	10 000	524.487	5.766	B2
7.500	10 000	573.969	7.652	B2
7.763	10 000	634.725	9.886	B2
8.000	10 000	690.299	11.949	B2
8.600	10 000	844.597	17.576	B2
8.800	10 000	900.317	19.563	B2
10.000	10 000	1280.928	32.517	B2
11.000	10 000	1656.101	44.571	B2
5.999	11 000	354.293	3.24	liquid
5.513	11 000	253.386	− 5.104	B1
6.499	11 000	394.352	1.846	B2
6.762	11 000	439.543	3.554	B2
7.263	11 000	536.250	7.180	B2

TABLE I. *(Continued.)*

ρ (g/cm^3)	T (K)	P (GPa)	u (kJ/g)	Phase
3.550	12 000	85.467	− 5.848	liquid
3.884	12 000	110.516	− 4.966	liquid
5.076	12 000	230.927	− 0.507	liquid
5.513	12 000	289.654	2.001	liquid
5.983	12 000	360.000	4.636	liquid
5.999	12 000	365.664	5.199	liquid
7.000	12 000	495.767	6.719	B2
7.263	12 000	547.867	8.659	B2
7.500	12 000	597.519	10.514	B2
7.763	12 000	657.558	12.694	B2
8.000	12 000	714.206	14.848	B2
8.600	12 000	869.705	20.309	B2
5.999	13 000	376.731	7.205	liquid
6.250	13 000	416.574	8.525	liquid
6.499	13 000	464.910	10.700	liquid
7.263	13 000	560.130	10.242	B2
7.500	13 000	610.393	12.034	B2
3.550	14 000	95.531	− 2.722	liquid
3.884	14 000	122.115	− 1.670	liquid
5.076	14 000	248.416	3.287	liquid
5.983	14 000	380.145	8.340	liquid
6.499	14 000	476.803	12.699	liquid
6.762	14 000	526.096	14.492	liquid

TABLE I. *(Continued.)*

ρ (g/cm^3)	T (K)	P (GPa)	u (kJ/g)	Phase
7.000	14 000	576.631	16.484	liquid
7.120	14 000	601.222	17.166	liquid
7.763	14 000	684.244	15.812	B2
8.000	14 000	740.152	17.815	B2
8.600	14 000	896.370	23.270	B2
3.550	16 000	106.030	0.667	liquid
3.884	16 000	134.544	1.711	liquid
5.076	16 000	263.800	6.646	liquid
5.983	16 000	401.422	12.272	liquid
6.499	16 000	498.251	16.521	liquid
6.762	16 000	550.359	18.546	liquid
7.000	16 000	599.647	20.480	liquid
7.263	16 000	659.139	22.693	liquid
7.500	16 000	714.822	24.940	liquid
8.600	16 000	923.810	26.535	B2
8.999	16 000	1038.641	30.363	B2
10.000	16 000	1363.492	41.004	B2
11.000	16 000	1741.790	52.876	B2
7.500	18 000	735.891	28.332	liquid
7.000	20 000	646.105	28.227	liquid
7.500	20 000	761.318	32.534	liquid
8.000	20 000	892.850	37.719	liquid
8.600	20 000	1065.248	44.100	liquid

[1] W. B. Hubbard and M. S. Marley, Icarus **78**, 102 (1989).
[2] S. Seager, M. Kuchner, C. A. Hier-Majumder, and B. Militzer, Astrophys. J. **669**, 1279 (2007).
[3] V. Stamenković, D. Breuer, and T. Spohn, Icarus **216**, 572 (2011).
[4] H. F. Wilson and B. Militzer, Phys. Rev. Lett. **108**, 111101 (2012).
[5] A. M. Dziewonski and D. L. Andersen, Phys. Earth Planet. Inter. **25**, 297 (1981).
[6] O. L. Anderson, Geodynamics Series **31**, 83 (2003).
[7] D. Valencia, R. J. O'Connell, and D. Sasselov, Icarus **181**, 545 (2006).
[8] N. Nettelmann, B. Holst, A. Kietzmann, M. French, R. Redmer, and D. Blaschke, Astrophys. J. **683**, 1217 (2008).
[9] A. B. Belonoshko, S. Arapan, R. Martoňák, and A. Rosengren, Phys. Rev. B **81**, 054110 (2010).
[10] B. Boates and S. A. Bonev, Phys. Rev. Lett. **110**, 135504 (2013).
[11] N. D. Drummond and G. J. Ackland, Phys. Rev. B **65**, 184104 (2002).
[12] A. R. Oganov, M. J. Gillan, and G. D. Price, J. Chem. Phys. **118**, 10174 (2003).
[13] A. Strachan, T. Çağin, and W. A. Goddard, III, Phys. Rev. B **60**, 15084 (1999).
[14] T. S. Duffy, R. J. Hemley, and H.-k. Mao, Phys. Rev. Lett. **74**, 1371 (1995).
[15] A. Zerr and R. Boehler, Nature **371**, 506 (1994).
[16] L. Zhang and Y. Fei, Geophys. Res. Lett. **35**, L13302 (2008).
[17] D. Alfè, Phys. Rev. Lett. **94**, 235701 (2005).
[18] R. S. McWilliams, D. K. Spaulding, J. H. Eggert, P. M. Celliers, D. G. Hicks, R. F. Smith, G. W. Collins, and R. Jeanloz, Science **338**, 1330 (2012).
[19] F. Coppari, R. F. Smith, J. H. Eggert, J. Wang, J. R. Rygg, A. Lazicki, J. A. Hawreliak, G. W. Collins, and T. S. Duffy, Nat. Geosci. **6**, 926 (2013).
[20] N. de Koker and L. Stixrude, Geophys. J. Int. **178**, 162 (2009).
[21] N. de Koker, Earth Planet. Sci. Lett. **292**, 392 (2010).
[22] N. de Koker, Phys. Rev. Lett. **103**, 125902 (2009).
[23] G. Kresse and J. Hafner, Phys. Rev. B **48**, 13115 (1993).
[24] G. Kresse and J. Hafner, Phys. Rev. B **49**, 14251 (1994).
[25] G. Kresse and J. Furthmüller, Phys. Rev. B **54**, 11169 (1996).
[26] P. Hohenberg and W. Kohn, Phys. Rev. **136**, B864 (1964).
[27] W. Kohn and L. J. Sham, Phys. Rev. **140**, A1133 (1965).
[28] N. D. Mermin, Phys. Rev. **137**, A1441 (1965).
[29] M. Born and R. Oppenheimer, Ann. Phys. **389**, 457 (1927).
[30] S. Nosé, J. Chem. Phys. **81**, 511 (1984).
[31] R. Armiento and A. E. Mattsson, Phys. Rev. B **72**, 085108 (2005).
[32] A. E. Mattsson, R. Armiento, J. Paier, G. Kresse, J. M. Wills, and T. R. Mattsson, J. Chem. Phys. **128**, 084714 (2008).
[33] D. M. Ceperley and B. J. Alder, Phys. Rev. Lett. **45**, 566 (1980).
[34] J. P. Perdew, K. Burke, and M. Ernzerhof, Phys. Rev. Lett. **77**, 3865 (1996).
[35] J. P. Perdew, A. Ruzsinszky, G. I. Csonka, O. A. Vydrov, G. E. Scuseria, L. A. Constantin, X. Zhou, and K. Burke, Phys. Rev. Lett. **100**, 136406 (2008).

[36] P. E. Blöchl, Phys. Rev. B **50**, 17953 (1994).
[37] A. Baldereschi, Phys. Rev. B **7**, 5212 (1973).
[38] H. J. Monkhorst and J. D. Pack, Phys. Rev. B **13**, 5188 (1976).
[39] D. C. Wallace, *Statistical Physics of Crystals and Liquids: A Guide to Highly Accurate Equations of State* (World Scientific Publishing Company, Singapore, 2002).
[40] M. J. Gillan, D. Alfe, J. Brodholt, L. Vočadlo, and G. D. Price, Rep. Prog. Phys. **69**, 2365 (2006).
[41] A. Togo, F. Oba, and I. Tanaka, Phys. Rev. B **78**, 134106 (2008).
[42] D. Alfè, Comput. Phys. Commun. **180**, 2622 (2009).
[43] K. Parlinski, J. Łażewski, and Y. Kawazoe, J. Phys. Chem. Solids **61**, 87 (2000).
[44] D. A. Greenwood, Proc. Phys. Soc. **71**, 585 (1958).
[45] R. Kubo, J. Phys. Soc. Jpn. **12**, 570 (1957).
[46] S. Mazevet, M. P. Desjarlais, L. A. Collins, J. D. Kress, and N. H. Magee, Phys. Rev. E **71**, 016409 (2005).
[47] M. P. Desjarlais, J. D. Kress, and L. A. Collins, Phys. Rev. E **66**, 025401(R) (2002).
[48] B. Holst, M. French, and R. Redmer, Phys. Rev. B **83**, 235120 (2011).
[49] M. Born and E. Wolf, *Principles of Optics, Electromagnetic Theory of Propagation, Interference and Diffraction of Light* (Cambridge University Press, New York, 2002).
[50] R. E. Stephens and I. H. Malitson, J. Res. Natl. Bur. Stand. **49**, 249 (1952).
[51] H.-k. Mao and R. J. Hemley, Proc. Natl. Acad. Sci. USA **104**, 9114 (2007).
[52] S. P. Marsh, *LASL Shock Hugoniot Data* (University of California Press, Berkeley, 1980).
[53] B. Svendsen and T. J. Ahrens, Geophysical Journal International **91**, 667 (1987).
[54] M. S. Vassiliou and T. J. Ahrens, Geophys. Res. Lett. **8**, 729 (1981).
[55] S. T. Weir, A. C. Mitchell, and W. J. Nellis, Phys. Rev. Lett. **76**, 1860 (1996).
[56] N. F. Mott, Philos. Mag. **24**, 1 (1971).
[57] A. S. Rao and R. J. Kearney, Phys. Status Solidi(b) **95**, 243 (1979).
[58] J. Heyd, G. E. Scuseria, and M. Ernzerhof, J. Chem. Phys. **118**, 8207 (2003).
[59] M. French, T. R. Mattsson, and R. Redmer, Phys. Rev. B **82**, 174108 (2010).
[60] M. French and R. Redmer, Phys. Plasmas **18**, 043301 (2011).
[61] M. D. Knudson, M. P. Desjarlais, R. W. Lemke, T. R. Mattsson, M. French, N. Nettelmann, and R. Redmer, Phys. Rev. Lett. **108**, 091102 (2012).
[62] S.-i. Karato, Icarus **212**, 14 (2011).